

# Compressed Ultrasound Signal Reconstruction using a Low-rank and Joint-sparse Representation Model

Miaomiao Zhang, Ivan Markovsky, Colas Schretter, Jan D’hooge\*

**Abstract**—With the introduction of very dense sensor arrays in ultrasound imaging, data transfer rate and data storage can become a bottle neck in ultrasound system design. To reduce the amount of sampled channel data, we propose a new approach based on the low-rank and joint-sparse model that allows to exploit the correlations between different ultrasound channels and transmissions. With this method, the minimum number of measurements at each channel can be lower than the sparsity in compressive sensing theory. The accuracy of the reconstruction is less dependent on the sparse basis. An optimization algorithm, based on the simultaneous direction method of multipliers, is proposed to efficiently solve the resulting optimization problem. Results on different datasets with different experimental settings show that the proposed method is better adapted to the ultrasound signals and can recover the image with fewer samples (*e.g.* 10% of the samples) than existing CS-based methods, while maintaining adequate image quality.

**Index Terms**—compressive sensing, matrix completion, low-rank and joint-sparse model, ultrasound imaging

## I. INTRODUCTION

ULTRASOUND (US) echography is one of the most used diagnostic imaging techniques as it is real-time, safe, low-cost and portable. Conventional ultrasound imaging is usually performed by scanning a medium using sequential focused beams, each firing allowing the reconstruction of one line of the final image, *i.e.* Single-Line-Transmission (SLT) imaging. A high-resolution image requires sufficient numbers of transmissions as well as a sampling rate that is significantly higher than the Nyquist rate of the signal [1]. Consequently, with such high sampling rate, and taking into account the number of transmissions and the number of transducer elements, the amount of sampled data can become enormous, which restricts the data storage and transportation in most of the commercial systems today. In this context, the recently introduced compressive sensing (CS) theory provides a promising way of reducing the amount of data. The CS theory shows that if a 1D signal of length  $M$  is sparse or has a sparse representation in a known basis with sparsity  $k$ , then it can be recovered from  $M_s = O(k \log M)$  incoherent samples [2]–[4].

Based on the CS theory, a number of strategies have been proposed to reduce the volume of US data [5]–[22]. Most of the proposed methods can be roughly grouped into

M. Zhang and J. D’hooge\* are with Laboratory of Cardiovascular Imaging and Dynamics, Department of Cardiovascular Sciences, KU Leuven, 3000 Leuven, Belgium. E-mail: jan.dhooge@uzleuven.be

I. Markovsky is with the Department ELEC, Vrije Universiteit Brussel (VUB), 1050 Brussels, Belgium.

C. Schretter is with the Department of Electronics and Informatics (ETRO), Vrije Universiteit Brussel, Pleinlaan 2, 1050 Brussel, Belgium.

two categories. The first allows for reducing the number of transmits by sparsely sampling the spatial domain and is useful for improving the frame rate [5]–[9]. Even when the number of transmissions is reduced, the amount of sampled data is still very large due to the high temporal sampling frequency. This motivates the second group of methods for reducing the sampling rate [10]–[22]. However, since the CS theory is performed on 1D signal (including the vectorized representation of 2D or multi-dimensional signal), the minimum number of required samples (*i.e.*  $M_s = O(k \log M)$ ) per line has to be respected. The above studies mainly look into the use of different sparse bases or measurement matrix in order to reduce the number of samples  $M_s$  and improve the accuracy of the reconstructed signal.

In US imaging, signals coming from individual sensor array elements are highly correlated particularly for elements that are physically nearby. Similarly, the signals from subsequent ultrasound transmit events (*i.e.* close in space and time) are highly correlated. To improve the performance of CS for multiple signals, new reconstruction algorithms were designed based on the assumption that all the 1D signals are jointly sparse in a known basis, which was referred to as distributed compressive sensing (DCS) [23]. To further reduce the number of samples, Basarab *et al.* [20] and Zhang *et al.* [24] applied the DCS framework to US imaging under the assumption that all the signals to reconstruct have the same sparse support in the 1D Fourier domain. This hypothesis is reasonable, since the radio frequency (RF) signals are bandlimited by the impulse response of the transducer. However, the DCS is an extension of CS, implying that the reconstruction accuracy of the DCS algorithm still depends on the choice of the sparse basis and the measurement matrix. Moreover, the number of measurements per signal cannot be lower than the sparsity  $k$ .

To further exploit the correlations in the spatio-temporal RF dataset, Jin *et al.* proposed to use a low-rank matrix completion (MC) method (*i.e.* ALOHA, annihilating filtered-based low-rank Hankel matrix approach) to reduce the number of transmissions in US signals [25]. Unlike CS, the MC theory directly performs the reconstruction on a matrix. It states that a full matrix, which is low rank, can be recovered exactly from a small number of randomly selected entries from the matrix when some conditions are met [26]. As such, MC provides a new way of reducing data size and has been applied to several fields, such as magnetic resonance imaging [27], radar imaging [28], fast magnetic resonance spectroscopy [29], multi-modal recognition [30] and others. However, because of the size of the pre-beamformed RF data, directly applying the MC theory on the pre-beamformed RF data matrix is time and memory

consuming.

In order to further reducing the sampling rate, we propose to use a low-rank and joint-sparse model to represent the US signal, which can overcome the sparsity limit of CS and simplify the MC model. This model has been used in hyperspectral imaging [31], [32], and multi-modal recognition [33]. The optimization problem in [31]–[33] was built to recover the original signal matrix. In this manuscript, to further reduce the sampling rate and improve the reconstruction accuracy, we reformulated the optimization problem to reconstruct the Fourier coefficients instead of the original signal matrix. Thus, the problem is much simplified because of the bandpass characteristic (*i.e.* joint-sparse in 1D Fourier domain) of the US signal. An algorithm based on simultaneous direction method of multipliers (SDMM) [34]–[36] is also proposed to solve the associate optimization problem.

The remainder of the paper is organized as follows. First, we formulate our problem as a convex optimization problem based on low-rank and joint-sparse model and proposed a SDMM-based algorithm to efficiently solve it in Section II. In Section IV, simulated and experimental results are provided to validate and evaluate the performance of the proposed approach. The discussion is provided in Section V, while the conclusions are drawn in Section VI.

## II. METHODOLOGY

The motivation to formulate a low-rank and joint-sparse model comes from the observation that the pre-beamformed US signals from different transducer elements are joint-sparse in the Fourier domain and also correlated between transmissions. Both properties imply that they show a low rank structure when represented as a matrix.

### A. Low-rank and joint-sparse model of the US signals

Let us rearrange all the received pre-beamformed RF data in a 2D matrix  $\mathbf{X} \in R^{M \times N}$ , where  $M$  is the number of samples along depth and  $N$  is the total number of RF signals (*i.e.* the number of transmissions multiply by the number of active elements for each transmission). For each channel,  $n = 1, 2, \dots, N$ , we denote  $\mathbf{x}_n$  as a vector signal of  $M$  samples. It is shown in [10], [14], [20] that the RF signal is sparse and also joint-sparse in the Fourier domain with a sparsity of  $k$  ( $k \ll M$ ), which means that each sample  $\mathbf{x}_n(m)$  can be modeled as a weighted sum of complex sinusoids at  $k$  discrete frequencies  $f_i$ ,  $1 \leq i \leq k$ , *i.e.*

$$\mathbf{x}_n(m) = \sum_{i=1}^k d_{i,n} e^{j2\pi f_i m} = \sum_{i=1}^k d_{i,n} y_i^m, \quad 0 \leq m < M \quad (1)$$

where for any  $i$  we define  $y_i = e^{j2\pi f_i}$ . In conventional CS-based methods, those frequencies  $f_i$  and sparsity  $k$  are unknown. But, in fact, because of the bandpass characteristic of the US transducer, **most of the energy of the Fourier spectrum is concentrated in  $\pm[f_c/2, 3f_c/2]$**  (*i.e.* the bandwidth of the transducer is 1), where  $f_c$  is the center frequency of the RF signal. Therefore, under such assumption, those frequencies  $f_i$  are known and  $k = M(2f_c/f_s)$ , where  $f_s$  is the

sampling frequency of the RF signal. Applying such relation to all the columns of  $\mathbf{X}$ , we can then express the 2D RF data  $\mathbf{X}$  in a matrix form as:

$$\mathbf{X} = \mathbf{Y}\mathbf{D} \quad (2)$$

with

$$\mathbf{Y} = \begin{pmatrix} 1 & 1 & \cdots & 1 \\ y_1 & y_2 & \cdots & y_k \\ \vdots & \vdots & \ddots & \vdots \\ y_1^{M-1} & y_2^{M-1} & \cdots & y_k^{M-1} \end{pmatrix}_{M \times k} \quad (3)$$

and

$$\mathbf{D} = \begin{pmatrix} d_{1,1} & d_{1,2} & \cdots & d_{1,N} \\ d_{2,1} & d_{2,2} & \cdots & d_{2,N} \\ \vdots & \vdots & \ddots & \vdots \\ d_{k,1} & d_{k,2} & \cdots & d_{k,N} \end{pmatrix}_{k \times N} \quad (4)$$

where  $\mathbf{Y}$  is a partial 1D Fourier matrix with frequencies  $f_i$  and  $\mathbf{D}$  is the Fourier coefficient matrix of  $\mathbf{X}$  corresponding to  $\mathbf{Y}$ . Since the maximum bandwidth of the RF signals is 1, some rows of  $\mathbf{D}$  maybe zeros (*i.e.* the real bandwidth of the acquired RF signal is smaller than 1). The above factorization form in (2) also implies a low-rank structure of  $\mathbf{X}$  with:

$$\text{rank}(\mathbf{X}) \leq k, \quad \text{when } k < N \quad (5)$$

where  $\text{rank}(\mathbf{X}) = k$  if and only if  $\mathbf{D}$  is full-rank (*i.e.* the  $k$  rows of  $\mathbf{D}$  are independent). In practice, thanks to the strong correlation between US signals, we have  $\text{rank}(\mathbf{X}) < k$  ([An example is given to show this relation in Appendix](#)). Thus,  $\mathbf{X}$  has a low-rank and joint-sparse structure when we have enough number of US channel signals, *i.e.*  $N > \text{rank}(\mathbf{X})$ . Fortunately, in the field of US, the above condition is generally satisfied with  $N \gg \text{rank}(\mathbf{X})$ , implying that the low-rank and joint-sparse property can be applied in US signal reconstruction.

### B. Signal reconstruction model

Assuming that the data is contaminated by random noise, the measurements  $\mathbf{B}$  can be modeled as :

$$\mathbf{B} = \mathbf{P}_\Omega(\mathbf{X}) + \mathbf{N}_e \quad (6)$$

where  $\Omega$  is a set of locations where the signal  $\mathbf{x}_n(m)$  is observed, *i.e.*  $\mathbf{x}_n(m)$  known if  $(m, n) \in \Omega$ .  $\mathbf{P}_\Omega(\mathbf{X})$  represents the corresponding values of  $\mathbf{X}$  in the locations of  $\Omega$ , *i.e.*  $\mathbf{P}_\Omega(\mathbf{X}) = \mathbf{P}_\Omega \cdot \mathbf{X}$ , where  $\mathbf{P}_\Omega$  is a matrix with 1 in the locations  $\Omega$  and 0 elsewhere.  $\mathbf{N}_e$  is the additive noise term. In these settings, the reconstruction problem thus amounts to obtain  $\mathbf{X}$  from (6), under the constraint that  $\mathbf{X}$  is low-rank and joint-sparse. This problem could be reformulated as an unconstrained optimization problem as in [37], [38]:

$$\hat{\mathbf{X}} = \arg \min_{\mathbf{X}} \|\mathbf{X}\|_* + \alpha \|\mathbf{Y}_t \mathbf{X}\|_{2,1} + \frac{1}{2\mu} \|\mathbf{B} - \mathbf{P}_\Omega(\mathbf{X})\|_F^2 \quad (7)$$

where  $\|\mathbf{X}\|_* = \sum_i \sigma_i$  is the sum of the singular values (*i.e.* the nuclear norm) that aims at imposing the low-rank property of  $\mathbf{X}$ . This assumption has been extensively used in Matrix

Completion, see [26], [40], [41];  $\mathbf{Y}_t$  is the adjoint operator of  $\mathbf{Y}$  with the relation  $\mathbf{Y}_t \mathbf{X} = \mathbf{D}$ . In our case,  $\mathbf{Y}_t$  and  $\mathbf{Y}$  are the Fourier and Inverse Fourier matrix with effective frequencies  $f_i$ ;  $\|\mathbf{D}\|_{2,1} = \sum_{i=1}^k \|\mathbf{d}^i\|_2$  (i.e. the  $\ell_{2,1}$  norm) that is used to explore the joint sparsity property of  $\mathbf{D}$  and  $\mathbf{d}^i$  denotes the  $i$ -th row of  $\mathbf{D}$  [39];  $\|\cdot\|_F$  is the Frobenius norm. The parameters  $\alpha$  and  $\mu$  give the trade-off among the nuclear norm term  $\|\mathbf{X}\|_*$ , the  $\ell_{2,1}$  norm term  $\|\mathbf{Y}_t \mathbf{X}\|_{2,1}$  and the data consistency term  $\|\mathbf{B} - \mathbf{P}_\Omega(\mathbf{X})\|_F^2$ . Fundamentally, we are looking for a 2D matrix with minimum rank and joint-sparsity subject to the acquired data. Thanks to the relation between  $\mathbf{X}$  and  $\mathbf{D}$  in (2) and the fact that  $\mathbf{Y}$  is a known full rank matrix, minimizing the nuclear norm of  $\mathbf{X}$  is the same as  $\mathbf{D}$ . Thus the above problem (7) could be reformulated as:

$$\hat{\mathbf{D}} = \arg \min_{\mathbf{D}} \|\mathbf{D}\|_* + \alpha \|\mathbf{D}\|_{2,1} + \frac{1}{2\mu} \|\mathbf{B} - \mathbf{P}_\Omega(\mathbf{YD})\|_F^2 \quad (8)$$

The objective function in (8) aims at estimating  $\mathbf{D}$  instead of  $\mathbf{X}$  directly from the acquired samples. It is worth to notice that  $\mathbf{D}$  is a  $k \times N$  matrix with  $k \ll M$ , which means the number of variables to be estimated in  $\mathbf{D}$  is  $\frac{M}{k}$  times less than  $\mathbf{X}$  and the problem (7) is much simplified. To solve the optimization problem in (8), we proposed hereafter an algorithm based on the simultaneous direction method of multipliers (SDMM) [34]–[36].

### C. Optimization and implementation details

In this section, we adapted the SDMM optimization framework (see Section II in [36] for more details) to solve the problem in (8). First, we reformulate (8) as the following constrained minimization problem:

$$\arg \min_{\mathbf{W}_1, \mathbf{W}_2, \mathbf{W}_3, \mathbf{D}} g_1(\mathbf{W}_1) + g_2(\mathbf{W}_2) + g_3(\mathbf{W}_3) \quad (9)$$

with

$$\left\{ \begin{array}{l} g_1(\mathbf{W}_1) = \|\mathbf{W}_1\|_* \\ g_2(\mathbf{W}_2) = \alpha \|\mathbf{W}_2\|_{2,1} \\ g_3(\mathbf{W}_3) = \frac{1}{2\mu} \|\mathbf{B} - \mathbf{P}_\Omega(\mathbf{W}_3)\|_F^2 \\ \mathbf{W}_1 = \mathbf{D} \\ \mathbf{W}_2 = \mathbf{D} \\ \mathbf{W}_3 = \mathbf{YD} \end{array} \right.$$

Using the above parametrization, the SDMM iteratively solves the above optimization problem as follows:

**Step 1:** aims at updating  $\mathbf{D}$  by:

$$\mathbf{D}^{s+1} = \arg \min_{\mathbf{D}} \frac{1}{2\gamma} \left\| \begin{pmatrix} \mathbf{b}_1^s \\ \mathbf{b}_2^s \\ \mathbf{b}_3^s \end{pmatrix} + \begin{pmatrix} \mathbf{I} \\ \mathbf{I} \\ \mathbf{Y} \end{pmatrix} \mathbf{D} - \begin{pmatrix} \mathbf{W}_1^s \\ \mathbf{W}_2^s \\ \mathbf{W}_3^s \end{pmatrix} \right\|_F^2 \quad (10)$$

where  $\mathbf{b}_1$ ,  $\mathbf{b}_2$  and  $\mathbf{b}_3$  are Lagrangian parameters that have the same dimensions as  $\mathbf{W}_1$ ,  $\mathbf{W}_2$  and  $\mathbf{W}_3$ , respectively.  $(\cdot)^s$  means the updated value of  $(\cdot)$  from the  $s$ -th iteration.  $\gamma > 0$  is a penalty parameter. (10) is a classical  $l_2$  norm minimization problem and can be efficiently solved by setting it to zero. Then the final solution of  $\mathbf{D}$  is:

$$\mathbf{D}^{s+1} = \frac{(\mathbf{W}_1^s - \mathbf{b}_1^s) + (\mathbf{W}_2^s - \mathbf{b}_2^s) + \mathbf{Y}_t(\mathbf{W}_3^s - \mathbf{b}_3^s)}{3} \quad (11)$$

**Step 2:** consists in solving  $\mathbf{w}_i$  using:

$$\begin{pmatrix} \mathbf{W}_1^{s+1} \\ \mathbf{W}_2^{s+1} \\ \mathbf{W}_3^{s+1} \end{pmatrix} = \arg \min_{\mathbf{w}_1, \mathbf{w}_2, \mathbf{w}_3} \left\{ \frac{1}{2\gamma} \left\| \begin{pmatrix} \mathbf{b}_1^s \\ \mathbf{b}_2^s \\ \mathbf{b}_3^s \end{pmatrix} + \begin{pmatrix} \mathbf{I} \\ \mathbf{I} \\ \mathbf{Y} \end{pmatrix} \mathbf{D}^{s+1} \right. \right. \\ \left. \left. - \begin{pmatrix} \mathbf{W}_1 \\ \mathbf{W}_2 \\ \mathbf{W}_3 \end{pmatrix} \right\|_F^2 + \sum_{i=1}^3 g_i(\mathbf{W}_i) \right\} \quad (12)$$

Due to the separate structure of (12), it can be solved by minimizing the three subproblems that correspond to the update of  $\mathbf{W}_1$ ,  $\mathbf{W}_2$  and  $\mathbf{W}_3$ , respectively.

**Step 2.1:** updating  $\mathbf{W}_1$ :

$$\begin{aligned} \mathbf{W}_1^{s+1} &= \arg \min_{\mathbf{W}_1} \|\mathbf{W}_1\|_* + \frac{1}{2\gamma} \|\mathbf{b}_1^s + \mathbf{D}^{s+1} - \mathbf{W}_1\|_F^2 \\ &= \arg \min_{\mathbf{W}_1} \gamma \|\mathbf{W}_1\|_* + \frac{1}{2} \|\mathbf{b}_1^s + \mathbf{D}^{s+1} - \mathbf{W}_1\|_F^2 \end{aligned} \quad (13)$$

This is the well-known Matrix Completion problem whose solution is given by shrinking the singular values of  $\mathbf{b}_1^s + \mathbf{D}^{s+1}$  [40], [42]:

$$\mathbf{W}_1^{s+1} = \mathbf{US}(\Sigma, \gamma)\mathbf{V}^T \quad (14)$$

where  $\mathbf{U}\Sigma\mathbf{V}^T$  is the Singular Value Decomposition (SVD) of  $\mathbf{b}_1^s + \mathbf{D}^{s+1}$ ,  $S(a, b) = \text{sgn}(a)(|a| - b)$  for  $|a| \geq b$  and zero otherwise.

**Step 2.2:** updating  $\mathbf{W}_2$ :

$$\begin{aligned} \mathbf{W}_2^{s+1} &= \arg \min_{\mathbf{W}_2} \alpha \|\mathbf{W}_2\|_{2,1} + \frac{1}{2\gamma} \|\mathbf{b}_2^s + \mathbf{D}^{s+1} - \mathbf{W}_2\|_F^2 \\ &= \arg \min_{\mathbf{W}_2} \alpha \gamma \|\mathbf{W}_2\|_{2,1} + \frac{1}{2} \|\mathbf{b}_2^s + \mathbf{D}^{s+1} - \mathbf{W}_2\|_F^2 \end{aligned} \quad (15)$$

Due to the separate structure of  $\ell_{2,1}$  norm, this problem could be solved by minimizing each row of  $\mathbf{W}_2$  separately [43]. Let  $\mathbf{P} = \mathbf{b}_2^s + \mathbf{D}^{s+1}$ ,  $\mathbf{p}^i$  and  $\mathbf{W}_2^{i,s+1}$  be the  $i$ -th row of matrices  $\mathbf{P}$  and  $\mathbf{W}_2^{s+1}$ , respectively. The closed form solution for each row of  $\mathbf{W}_2^{s+1}$  is given as follows:

$$\mathbf{W}_2^{i,s+1} = \left( 1 - \frac{\alpha \gamma}{\|\mathbf{p}^i\|_2} \right)_+ \mathbf{p}^i \quad (16)$$

where  $(\mathbf{v})_+$  is a vector with entries receiving values  $\max(v_i, 0)$ .

**Step 2.3:** updating  $\mathbf{W}_3$ :

$$\begin{aligned} \mathbf{W}_3^{s+1} &= \arg \min_{\mathbf{W}_3} \frac{1}{2\mu} \|\mathbf{B} - \mathbf{P}_\Omega(\mathbf{W}_3)\|_F^2 \\ &\quad + \frac{1}{2\gamma} \|\mathbf{b}_3^s + \mathbf{YD}^{s+1} - \mathbf{W}_3\|_F^2 \end{aligned} \quad (17)$$

This equation could be easily solved by setting the first-order derivative equal to zero. Furthermore,  $\mathbf{W}_3^{s+1}$  could be expressed as a summation of two sub-matrices  $\mathbf{P}_\Omega(\mathbf{W}_3^{s+1})$  and  $\mathbf{P}_{\tilde{\Omega}}(\mathbf{W}_3^{s+1})$ , where  $\mathbf{P}_{\tilde{\Omega}}(\mathbf{W}_3^{s+1})$  represents the corresponding

values of  $\mathbf{W}_3^{s+1}$  out of the locations of  $\Omega$ . The final solution of  $\mathbf{W}_3^{s+1}$  is given below:

$$\mathbf{W}_3^{s+1} = \mathbf{P}_\Omega(\mathbf{W}_3^{s+1}) + \mathbf{P}_{\tilde{\Omega}}(\mathbf{W}_3^{s+1}) \quad (18)$$

with

$$\begin{cases} \mathbf{P}_\Omega(\mathbf{W}_3^{s+1}) = (\gamma \mathbf{P}_\Omega(\mathbf{B}) + \mu \mathbf{P}_\Omega(\mathbf{b}_3^s + \mathbf{YD}^{s+1})) / (\gamma + \mu) \\ \mathbf{P}_{\tilde{\Omega}}(\mathbf{W}_3^{s+1}) = \mathbf{P}_{\tilde{\Omega}}(\mathbf{b}_3^s + \mathbf{YD}^{s+1}) \end{cases} \quad (19)$$

**Step 3:** Finally, the Lagrange parameters are updated as:

$$\begin{pmatrix} \mathbf{b}_1^{s+1} \\ \mathbf{b}_2^{s+1} \\ \mathbf{b}_3^{s+1} \end{pmatrix} = \begin{pmatrix} \mathbf{b}_1^s \\ \mathbf{b}_2^s \\ \mathbf{b}_3^s \end{pmatrix} + \begin{pmatrix} \mathbf{I} \\ \mathbf{I} \\ \mathbf{Y} \end{pmatrix} \mathbf{D}^{s+1} - \begin{pmatrix} \mathbf{W}_1^{s+1} \\ \mathbf{W}_2^{s+1} \\ \mathbf{W}_3^{s+1} \end{pmatrix} \quad (20)$$

To conclude, the proposed SDMM-based numerical scheme for solving (8) is summarized in Algorithm 1.

---

#### Algorithm 1 Proposed algorithm for solving (8)

---

**Input:**  $\mathbf{B}, \mathbf{Y}, \mathbf{P}_\Omega, \gamma, \alpha, \mu$   
**Initialization:**  $\mathbf{b}_i^s, \mathbf{W}_i^s, i = 1, 2, 3$   
**while** not converged **do**  
 $\mathbf{D}^{s+1} \leftarrow \mathbf{b}_i^s, \mathbf{W}_i^s \quad \Leftrightarrow$  update  $\mathbf{D}^{s+1}$  using (11)  
 $\mathbf{W}_1^{s+1} \leftarrow \mathbf{b}_1^s, \mathbf{D}^{s+1} \quad \Leftrightarrow$  update  $\mathbf{W}_1^{s+1}$  using (14)  
 $\mathbf{W}_2^{s+1} \leftarrow \mathbf{b}_2^s, \mathbf{D}^{s+1} \quad \Leftrightarrow$  update  $\mathbf{W}_2^{s+1}$  using (16)  
 $\mathbf{W}_3^{s+1} \leftarrow \mathbf{b}_3^s, \mathbf{D}^{s+1} \quad \Leftrightarrow$  update  $\mathbf{W}_3^{s+1}$  using (18)  
 $\mathbf{b}_i^{s+1} \leftarrow \mathbf{b}_i^s, \mathbf{D}^{s+1}, \mathbf{W}_i^{s+1} \quad \Leftrightarrow$  update  $\mathbf{b}_i^{s+1}$  using (20)  
**end while**  
**Output:**  $\mathbf{D}$

---

### III. EXPERIMENTS

The performance of the proposed low-rank and joint-sparse method is evaluated on conventional SLT images. First, we test our algorithm on linear images to confirm that the proposed low-rank and joint-sparse model is well adapted to US RF signals and to contrast its performance to two CS-based methods introduced in Section III-A. Then, the proposed method is also evaluated on SLT sectorial images of the heart *in vivo* and compared with the conventional CS method for both RF and In-phase and Quadrature (IQ) datasets. All the signals are uniformly randomly sampled with different sampling rates (SR).

#### A. CS-based methods for comparison

The CS theory allows the reconstruction of a signal  $v \in R^M$  from a small number of measurements  $b \in R^c, c < M$  with the following relation:

$$b = \Phi \Psi v + e = Av + e \quad (21)$$

where  $A = \Phi \Psi$ , is a  $c \times M$  full rank matrix,  $\Phi$  is a  $c \times M$  sampling matrix,  $\Psi$  is a  $M \times M$  sparse basis,  $v$  is the corresponding coefficients and  $e$  represents a noise term with bounded energy  $\|e\|_2 \leq \varepsilon$ . The reconstruction problem aims at recovering  $v$  from  $b$ . Once  $v$  is estimated, the signal can be computed by  $\Psi v$ .

*1) Conventional CS method:* When  $v$  is sparse, the above reconstruction can be performed by solving the following minimization problem [44]:

$$\hat{v} = \arg \min \|v\|_1 \text{ subject to } \|b - Av\|_2 \leq \varepsilon \quad (22)$$

In each case of the testing datasets, the conventional CS reconstruction was performed on each RF signal individually. To be consistent with the proposed method, we used a standard DFT (Discrete Fourier Transform) matrix as the sparse basis  $\Psi$ . The reconstruction problem (22) was solved through the  $\ell_1$  minimization using the spectral projected-gradient algorithm SPGL1 [45] with  $\varepsilon = 1e^{-12}$ .

*2) Method proposed by Schretter et al. :* Instead of using a standard basis  $\Psi$  and assuming  $v$  is sparse, Schretter et al. proposed to model the final B-mode image as being composed of a linear combination of independent overlapping imaging elements [46]. Therefore, the raw RF measurements of one transmission can be decomposed into a small set of system point spread functions (PSFs). Thus  $\Psi$  is a collection of all PSFs in one transmission (please refer to [46] for detailed description) and the signal  $\Psi v$  to reconstruct is a vectorized representation of all the received raw signals for one transmission. The corresponding coefficient  $v$  could be obtained by solving the following approximation problem:

$$\hat{v} = \arg \min \|b - Av\|_2 \quad (23)$$

For SLT linear images, since each transmission has the same setting, those PSFs used to form  $\Psi$  are the same for all the transmissions. In this paper, we did the same as in [46] to compute PSFs using the ultrasound simulation package Field II [47]. The reconstruction problem (23) was solved by least squares regression (minimum  $l_2$ -norm residuals) with solution:

$$\hat{v} = [A^T A]^{-1} A^T b \quad (24)$$

#### B. Reconstruction protocol

For all the tests, each reconstructed image was obtained from the following protocol.

- i) Original raw RF signals of 1 image were acquired using SLT transmission scheme at different directions and rearranged as a matrix  $\mathbf{X}$ ;
- ii) Those signals were down-sampled at positions  $\mathbf{P}_\Omega$  (or  $\Phi$  in CS-based methods) to get the measurements  $\mathbf{B}$ ;
- iii) Then  $\mathbf{B}$  was processed either using the proposed method or the compared methods in Section III-A to reconstruct the full signal matrix  $\hat{\mathbf{X}}$ ;
- iv) The original RF signals  $\mathbf{X}$  and the estimated  $\hat{\mathbf{X}}$  were then beamformed using Delay-and-Sum (DAS) and the corresponding envelope images were derived through a Hilbert transform;
- v) The normalized envelope image was gamma-compressed using gamma = 0.3 as in [48] and finally converted into an 8-bit grayscale B-mode image.

### C. Evaluation metrics

To quantify the reconstruction error, the normalized root-mean-square error (NRMSE) of the beamformed RF image was calculated as in [5],

$$\text{NRMSE} = \frac{\sqrt{\frac{1}{M_b N_f} \sum_{b=1}^{M_b} \sum_{f=1}^{N_f} (I'(b, f) - I(b, f))^2}}{\max_{b,f} |I(b, f)|} \quad (25)$$

where  $I(b, f)$  and  $I'(b, f)$  denote the beamformed RF image from the original dataset and recovered dataset using the proposed method or the method of Schretter *et al.*  $M_b$  and  $N_f$  are the numbers of samples along depth and lateral directions of the image.

The image quality was also assessed from the image contrast at different regions of the image. The contrast was measured from the B-mode images using the following classical contrast-to-noise-ratio (CNR):

$$\text{CNR} = 20 \log_{10} \frac{|\mu_t - \mu_b|}{\sqrt{(\sigma_t^2 + \sigma_b^2)/2}} \quad (26)$$

where  $\mu_t$  and  $\mu_b$  ( $\sigma_t^2$  and  $\sigma_b^2$ ) are the means (variances) of the gray levels in the target and background region, respectively.

### D. Linear imaging setup

For comparison purposes, the same simulated and experimental settings were used as Schretter *et al.* in [46]. The parameters of acquisitions are shown in Table I. A numerical phantom, which contains five high-scattering point sources, five higher scattering regions and five regions without scatterers (See Fig. 2), was used to simulate the ground-truth channels data in Field II [47]. The *in vitro* experiment data was acquired using a Prosonic L14-5W/60 linear probe on a CIRS 054GS general purpose phantom.

TABLE I  
LINEAR IMAGE EXPERIMENTAL SETTINGS

Parameters	Simulation	Acquisition
Center frequency ( $f_c$ )	3.5 MHz	7 MHz
Sampling frequency ( $f_s$ )	25 MHz	40 MHz
Focal depth	60 mm	30 mm
Number of probe elements	192	128
Elements width	0.44 mm	0.46 mm
Elements height	5 mm	4 mm
Elements kerf	0.05 mm	0.012 mm
Number of active elements in transmission	64	32
Number of active elements in reception	64	32
Number of transmissions	100	97
Apodization in reception	Hanning	Hanning

### E. Sectorial imaging setup

The *in vivo* cardiac data was collected from a healthy volunteer and the experiment was performed using a fully programmable ultrasound system (HD-PULSE [49]) equipped with a commercially available Samsung phased array probe P2-5AC (64 elements, center frequency of 3.5 MHz, bandwidth of 60%). All signals were sampled at 25MHz. The focal depth of the SLT transmissions was set at 50 mm and steering angles from  $-35^\circ$  to  $35^\circ$  in  $1^\circ$  steps were made, resulting in

71 transmissions. No apodization was used in transmission or reception. All the backscattered RF data was acquired first, then it was demodulated with a sampling frequency of 3.57 MHz to get the corresponding IQ data, *i.e.* down sample factor is 7.

## IV. RESULTS

For all the experiments below, the proposed algorithm stopped when the convergence criterion  $\eta = ||\mathbf{D}^s - \mathbf{D}^{s-1}|| / ||\mathbf{D}^{s-1}|| < 5 \times 10^{-4}$  was satisfied, the initial values of  $(\mathbf{b}_i^s, \mathbf{W}_i^s, i = 1, 2, 3)$  are zeros and the other parameters  $\gamma, \alpha, \mu$  were obtained through cross validation. This resulted in these parameters to be set to  $\{\gamma, \alpha, \mu\} = \{10, 0.1, 10^{-6}\}$  for the linear simulated images and  $\{\gamma, \alpha, \mu\} = \{1, 0.1, 10^{-6}\}$  for the linear experimental images. Then for sectorial images,  $\{\gamma, \alpha, \mu\} = \{1, 0.01, 10^{-6}\}$  and  $\{\gamma, \alpha, \mu\} = \{1, 1, 10^{-6}\}$  are used for both RF and IQ datasets, respectively. The procedure of cross-validation and the influence of these parameters on the results are further investigated in Section IV-A2. The bandwidth of all the US datasets was assumed to be 1 to determine the first dimension of  $\mathbf{D}$ , *i.e.* the estimated sparsity  $k$  of the RF signal in Fourier basis. Those quantitative results (*i.e.* NRMSE and CNR) are the mean values of five experiments.

### A. Linear images

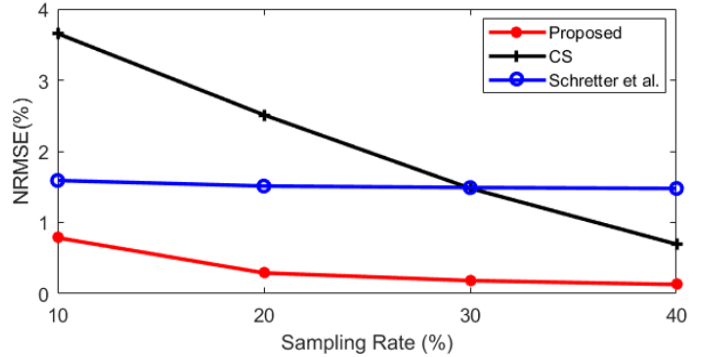


Fig. 1. Normalized root-mean-square error (NRMSE) for the proposed method, the CS method and the method of Schretter *et al.* with different sampling rates.

1) *Simulation results:* Figure 1 plots the NRMSE of the beamformed RF images with different sampling rates (SR) for the simulated phantom (see Figure 2). Firstly, it can be seen that the proposed method outperforms the other two methods for all sampling rates. In particular, it can be observed that even with 10% of samples, the proposed approach can almost totally recover the whole image with an error less than 1% while the conventional CS method has an error of about 4%. It is worth to note that, for this dataset, the sparsity of the signal  $k$  is about  $M \frac{2f_c}{f_s} = 28\% M$ , where  $M$  is the number of time samples of the full signal, *i.e.* the sparsity is about 28% of the signal length. This explains the phenomenon that the NRMSE of conventional CS method increased significantly for sampling rates of 10% and 20%. In other words, the sampling rate cannot be lower than 28% for CS method,

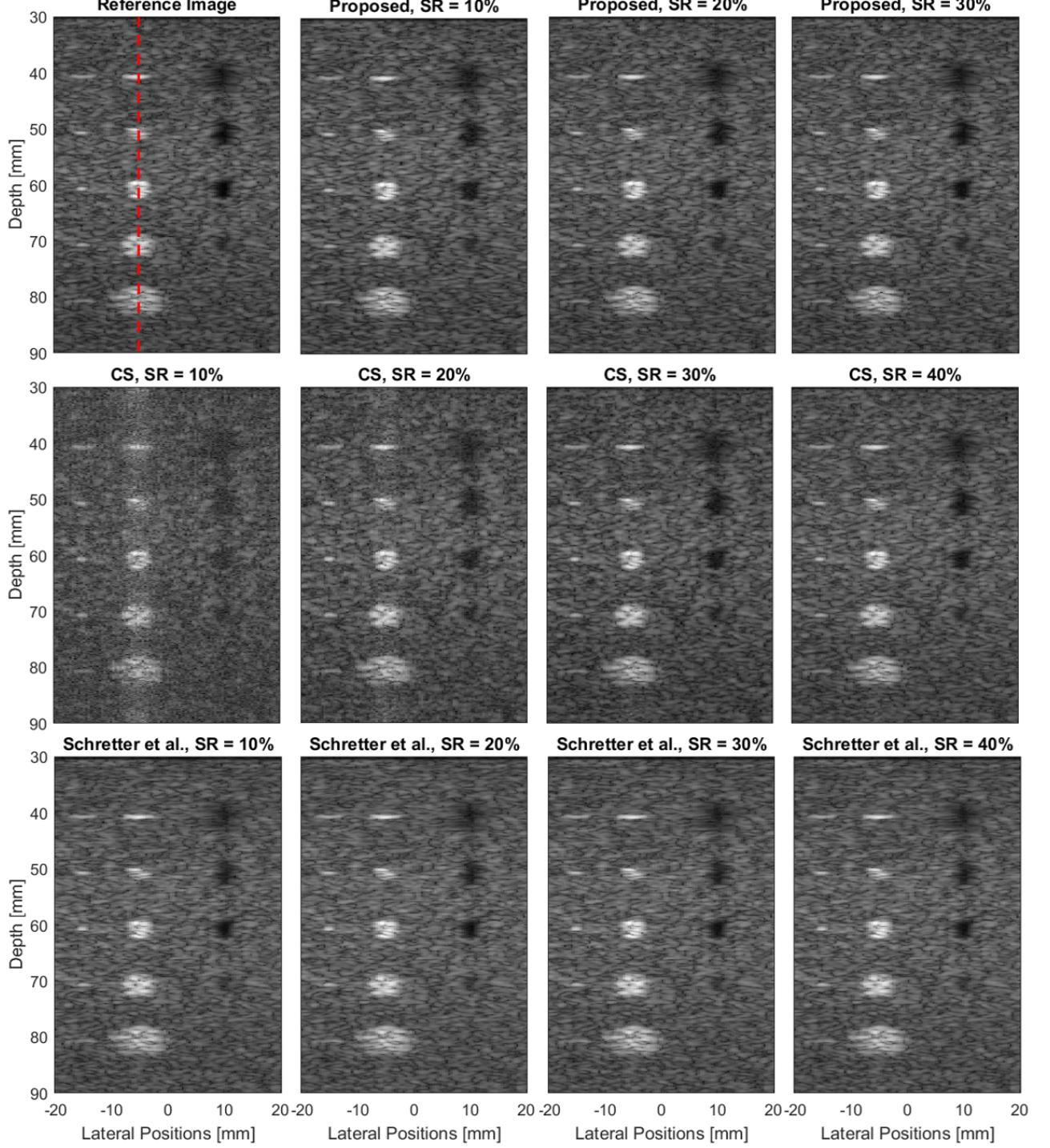


Fig. 2. Reference B-mode image of simulated phantom and the images reconstructed using the three approaches with different sampling rate. The red dash line in the reference image represents the line used in Fig.3.

while the proposed method can almost perfectly recover the whole signal with only 10% samples. Moreover, compared to the Nyquist frequency  $4f_c = 14$  MHz, the sampling frequency of the proposed method is about  $0.1f_s = 2.5$  MHz, which significantly reduce the amount of sampled channel data. Additionally, the NRMSE decreases as the sampling rate increases for the proposed method and conventional CS

method while it is sampling rate invariant for the method of Schretter *et al.* This behavior can be explained by the fact that the method used by Schretter *et al.* is a least square problem (as shown in Eq.(24)). When the least-square problem is well posed, increasing the number of measurements does not significantly improve the image quality. In other words, the proposed approach is more adapted to US signals. Figure

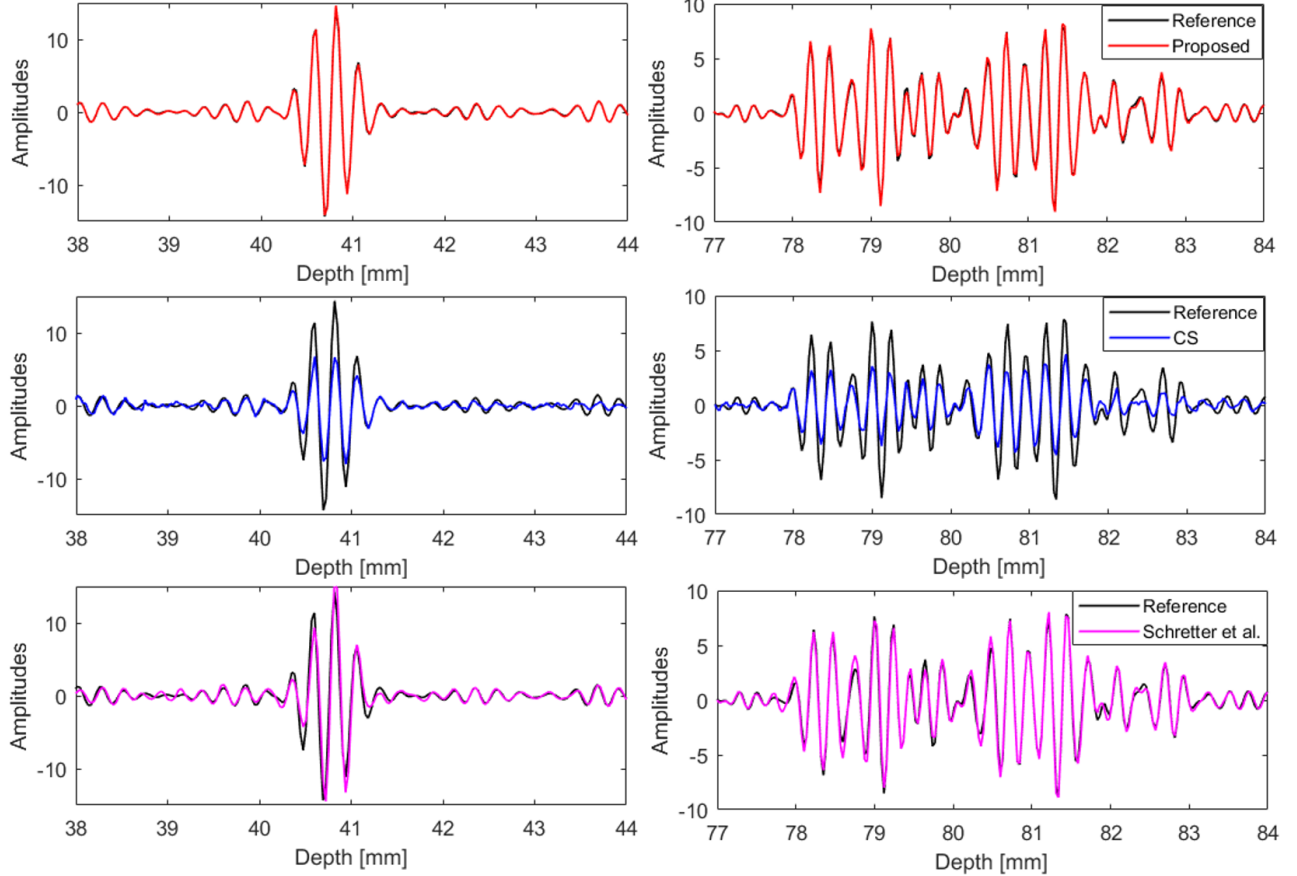


Fig. 3. Zoomed-in comparisons of the red dash line in the reference image and the recovered images from the three methods using 20% of data samples.

2 displays the corresponding images reconstructed from the proposed method, the conventional CS method and Schretter *et al.* for different sampling rates. Visually, strong artifacts appear for the images reconstructed by the conventional CS method with 10% and 20% samples. All the other reconstructed images are quite similar and close to the reference image. The 1% difference in NRMSE for the proposed method and the method of Schretter *et al.* cannot be seen. Therefore, we show in Figure 3 the difference of part of the red dash line in the reference image and the images reconstructed by the three approaches with 20% of samples. As can be seen, the proposed approach can recover the signal more accurately, while the CS method and the method of Schretter *et al.* have larger differences in terms of amplitudes and phase. This is consistent with the observations in Figure 1.

2) *Sensitivity of the parameters:* It is obvious that the input parameters (*i.e.*  $\gamma, \alpha, \mu$ ) of Algorithm 1 and the tolerance of convergence criterion  $\eta$  have impact on the quality of reconstruction. Given a certain convergence tolerance (*e.g.*  $\eta < 5 \times 10^{-4}$  in this paper), these parameters  $(\gamma, \alpha, \mu)$  are obtained through a cross-validation process: First  $\alpha$  and  $\mu$  are fixed and  $\gamma$  is optimized to find the smallest reconstruction error (*i.e.* NRMSE), where  $\alpha$  is set to 0 to find the best  $\gamma$  to minimizing the low-rank term of  $\mathbf{D}$ ,  $\mu = 10^{-6}$  to ensure the small error caused by the data consistency term. Then using this optimal value of  $\gamma$  and  $\mu = 10^{-6}$ ,  $\alpha$  is optimized to find the smallest

reconstruction error. Finally, using the optimal values of  $\gamma$  and  $\alpha, \mu$  is optimized to find the smallest reconstruction error. Figure 4 shows the influence of these parameters  $\gamma, \alpha$  and  $\mu$  on the reconstruction results (*i.e.* NRMSE) using the simulated dataset. It can be observed that the three parameters have a similar effect on reconstruction quality for different sampling rates implying that a single sampling rate can be investigated to understand their impact. In particular, the best results are obtained for  $\gamma \in [0.1, 10]$  and within this range, the choice of  $\gamma$  has little impact on the reconstruction quality. This can be explained by the fact that  $\gamma$  is an auxiliary parameter used in the SDMM framework, it mainly affects the convergence speed of the proposed algorithm. The bigger the value of  $\gamma$ , the faster the convergence. However, since  $\gamma$  is also used in the three sub-optimization problems of *Step 2*, it influences the reconstruction results implying that when taken too large it negatively affects the reconstruction quality. The other two parameters  $\alpha$  and  $\mu$  provide the compromise among the three terms of (8). The best results are obtained for  $\alpha \leq 10$  and  $\mu \leq 10^{-5}$ , corresponding to a small weight of the  $\ell_{21}$  norm term and an important weight of the data consistency term. Since the joint-sparsity property of  $\mathbf{D}$  has been used in (1) to select the effective frequencies of each  $\mathbf{d}_n$ , the weight of the  $\ell_{21}$  term is actually proportional to the difference between the real bandwidth of the signal and 1. If the real bandwidth is 1, only minimizing the low-rank property of the data is enough

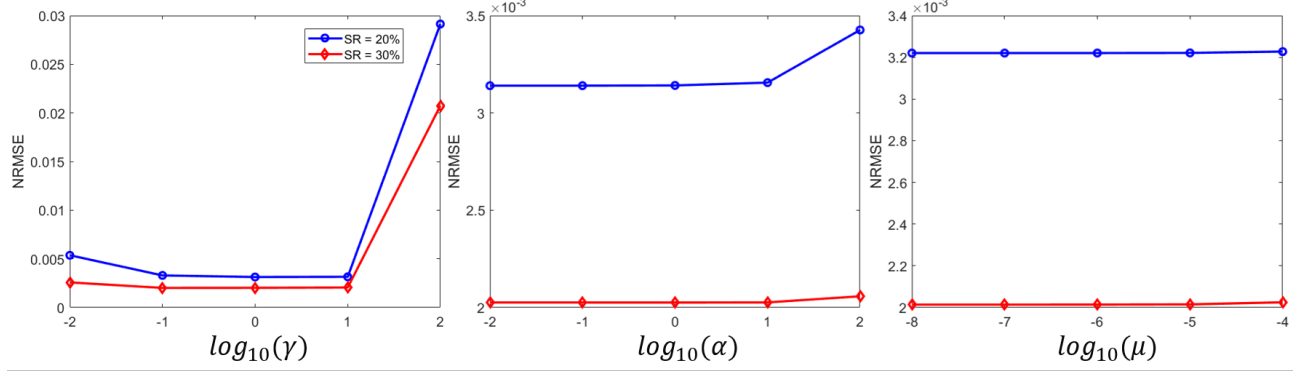


Fig. 4. The impact of  $\gamma$ ,  $\alpha$  and  $\mu$  on the performance of proposed method in Figure 2.

and  $\alpha = 0$ . Otherwise, there is a weight of the  $\ell_{21}$  norm term, *i.e.*  $\alpha > 0$ . Because of the small difference between the real bandwidth and 1,  $\alpha$  is small and cannot be bigger than a certain value (*e.g.* 10 in this experiment). The data consistency term only has influence on the sampled positions of the reconstructed signal which, in the best case, exactly match the observed samples. As such, beyond a certain value of  $\mu$  (*i.e.*  $1e^{-5}$  in this experiment), the choice of  $\mu$  has almost no impact on the results. Based on this sensitivity analysis, these parameters were set to  $\{\gamma, \alpha, \mu\} = \{10, 0.1, 1e^{-6}\}$  for the remainder of the liner image study.

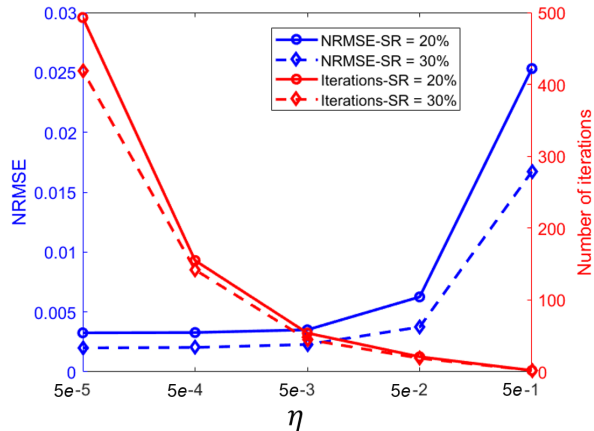


Fig. 5. The impact of the stop criterion  $\eta$  on the performance of proposed method in Figure 2.

Once the input parameters are fixed, the final optimization result is only influenced by the stop criterion of the algorithm. Figure 5 shows the impact of the stopping condition on the performance of the proposed algorithm. Obviously, a more strict stopping condition needs more iterations and results in a better result (*i.e.* small NRMSE). It also can be seen that when the convergence tolerance  $\eta$  is smaller than  $5 \times 10^{-3}$ , there is a little further gain in reconstruction quality while the number of iterations is significantly increased. In this paper, a strict stopping condition tolerance of  $5 \times 10^{-4}$  was therefore used to guarantee the optimized result for all experiments. However, if both the reconstruction error and the reconstruction time

(*i.e.* the number of iterations) are considered, a tolerance of  $\eta < 5 \times 10^{-3}$  seems to be a good trade-off.

**3) Experimental results:** Figure 6 presents the B-mode images reconstructed by the three approaches for different sampling rates. As can be seen, with 10% of samples, strong artifacts appear for conventional CS method and the method of Schretter *et al.* fails, while the proposed approach can recover the image accurately. **The method of Schretter *et al.* fails because of the insufficient number of samples, which results in a non-invertible Gram matrix  $[A^T A]$  in Eq.(24).** This aspect could be improved by using a dictionary with less number of PSFs or swapping the left Moore-Penrose pseudoinverse for a right-sided one. Visually, the other successfully reconstructed images look very similar to the reference image as in simulation. The quality of the reconstructed images was then quantitatively evaluated by CNR. The hyperechoic and background region used in the CNR calculation are marked with red and yellow rectangular boxes in Figure 6. The CNRs of the three methods for different sampling rates are shown in Table II. The proposed method and the method of Schretter *et al.* yield very similar results with the reference image (*i.e.* less than 0.1 dB difference), while the CS method produces a much lower CNR with 10% and 20% samples. This can be explained by the fact that the number of samples is less than the sparsity  $k$ .

TABLE II  
CNR ASSESSMENT FOR LINEAR SCAN EXPERIMENTAL DATA

Methods	Reference CNR	Sampling Rate			
		10%	20%	30%	40%
Proposed		7.02	7.03	7.08	7.09
CS		5.54	6.51	6.93	6.96
Schretter <i>et al.</i>		-	7.17	7.13	7.05

### B. Sectorial images

A direct comparison with the method of Schretter *et al.* was not performed as the dictionary used in this method is not suited for this scan geometry. For conventional CS method, it has been shown that strong artifacts would appear when the number of samples is lower than the sparsity  $k$ . In addition, the sparsity  $k$  in Fourier basis is almost the same as the full number of samples  $M$  for IQ dataset. Therefore, in this

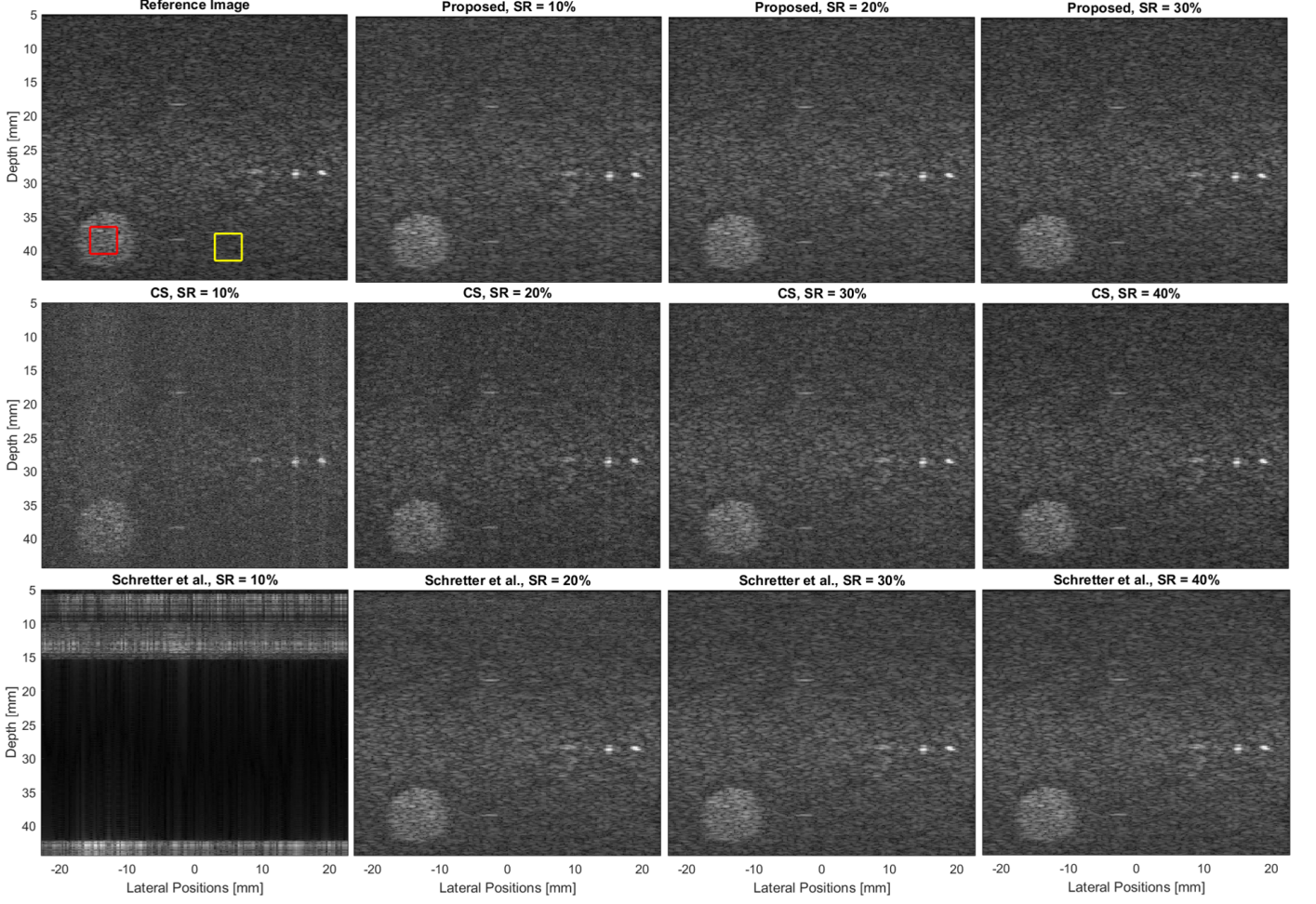


Fig. 6. Original B-mode image and the images reconstructed using the three approaches with different sampling rates. The red and yellow block in the reference image represent the regions used to compute CNR.

section, only the proposed method was evaluated for both RF and IQ datasets.

1) *Application on RF data:* The reconstructed images are shown in Figure 7 for different sampling rates. Two different regions of target and background for computing CNR are highlighted by the red and yellow boxes as T1, T2 and B1, B2. Table III gives the corresponding CNR assessment. It is obvious to see that strong artifacts appear for the reconstructed image with a sampling rate of 5%, corresponding to a reduction in CNR of about 2.5 dB. However, when the sampling rate increases, the artifacts disappear and the CNR improves, resulting in images visually very similar to the reference image. Unlike results obtained in the liner scan, there is an obvious degradation of CNR (*i.e.* 0.73 dB) for the cardiac image reconstructed from 10% of samples. This could be explained by many aspects, such as the higher measurement noise of the acquisition system, the motion-related artifacts of the *in vivo* heart and the sectorial transmission scheme. All these aspects lead to a poorer low-rank property of the original data matrix. Nevertheless, both the visual impression and the CNR results show the ability of our method to recover the image from fewer samples (*i.e.* 20% here) while maintaining almost the same image quality.

TABLE III  
CNR ASSESSMENT OF THE PROPOSED METHOD FOR CARDIAC RF DATA

Regions	Reference CNR	Sampling Rate				
		5%	10%	20%	30%	40%
T1 & B1	9.83	7.13	9.10	9.80	9.82	9.83
T2 & B2	9.07	6.63	8.3	9.11	9.17	9.15

2) *Application on IQ data:* Figure 8 displays the images reconstructed from the IQ dataset using the proposed method with different sampling rates. The corresponding CNRs were also measured and shown in Table IV. Compared to the RF dataset results, the reference CNR changed a little bit (around 0.3 dB), which may be caused by the low-pass filter that we used during the IQ demodulation process. As shown in table IV, the CNR increases with the sampling rate. If we assume that a difference in CNR between the reconstructed image and the reference image of around 0.1 dB means no degradation in image quality, the proposed method can reconstruct the original image with 70% of the IQ samples. Taking into account the down sample factor (*i.e.* 7) in IQ demodulation and a sampling rate of 70% on the IQ data, the final amount of data is about 10% of the original acquired signals, which

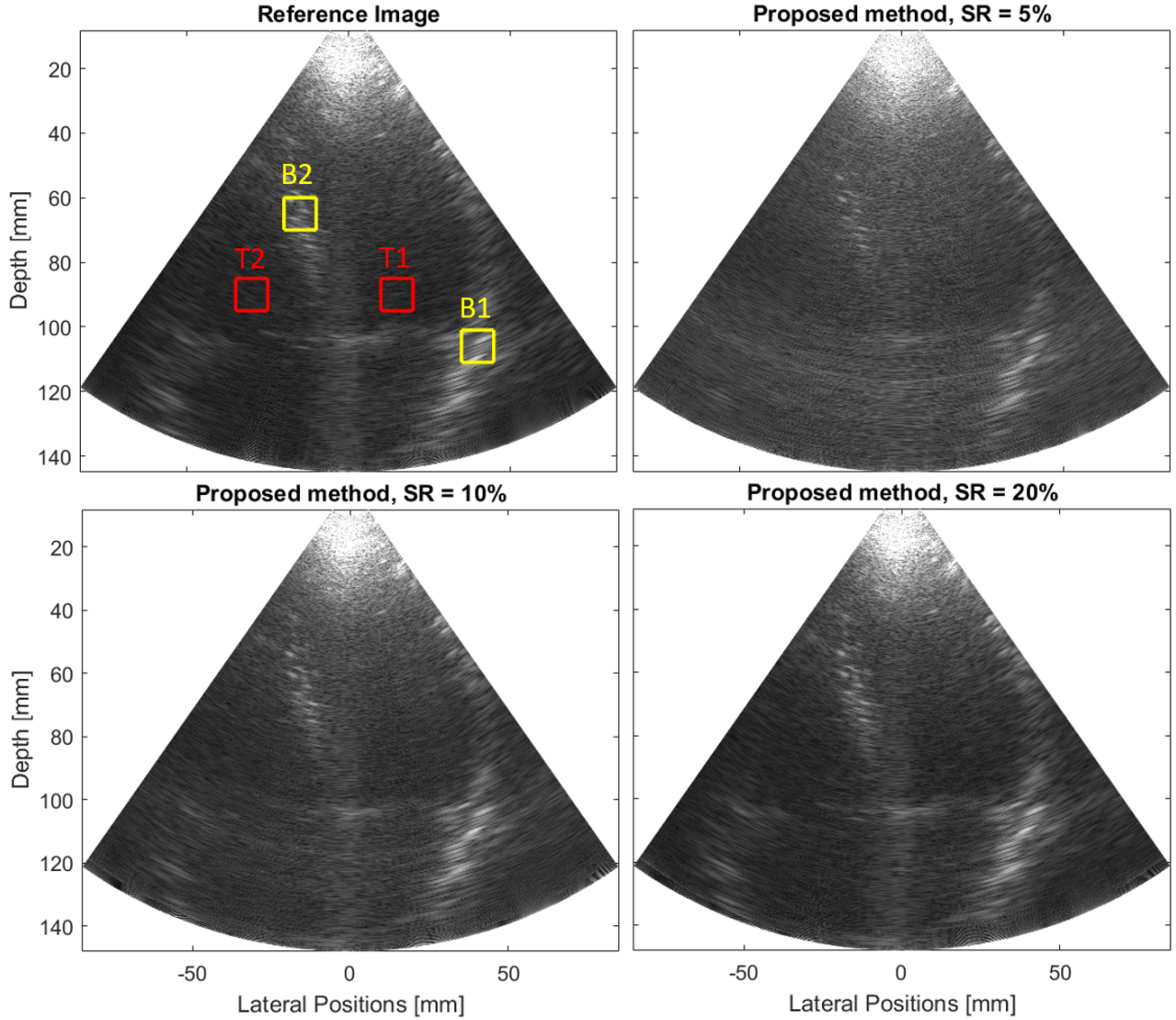


Fig. 7. Original *in vivo* cardiac image and the images reconstructed by the proposed method with different sampling rates. The red and yellow block in the reference image represent the regions used to compute CNR.

gains a better data compression rate than RF data. This could be explained by the fact that only half of the Fourier spectrum is used in IQ dataset, leading to a better low-rank property of the data matrix. In addition, it is worth to notice that the sampling frequency of the IQ data is almost the same as the center frequency (3.5 MHz). As a result, the estimation of  $\mathbf{D}$  in (8) does not simplify the problem, because  $\mathbf{D}$  is the same size as  $\mathbf{X}$  in (7) for IQ data.

TABLE IV  
CNR ASSESSMENT OF THE PROPOSED METHOD FOR CARDIAC  
IQ DATA

Regions	Reference CNR	Sampling Rate				
		30%	40%	50%	60%	70%
T1 & B1	9.52	8.88	9.30	9.43	9.54	9.58
T2 & B2	9.49	8.40	8.79	8.81	9.27	9.34
<b>Overall Sampling Rate</b>	<b>4.3%</b>	<b>5.7%</b>	<b>7.1%</b>	<b>8.6%</b>	<b>10%</b>	

## V. DISCUSSION

### A. Performance of the proposed approach

In this study, we proposed to use a low-rank and joint-sparse model to represent US signals and an efficient optimization algorithm to further reduce the sampling rate. Unlike existing strategies, the proposed method allows exploring the correlations between different channels and transmissions and the performance of the algorithm is less dependent on the sparse basis. In addition, the proposed approach simultaneously reconstructs the whole data matrix instead of reconstructing the data channel by channel. The results obtained from different datasets revealed that the proposed approach can reduce the sampling rate by 80-90% while keeping adequate image quality.

Compared to the strong artifacts of CS method and the failure of Schretter *et al.* in Figure 6 at 10% of sampling rate, the proposed approach achieves almost the same image quality as the reference image with a reduction of CNR less

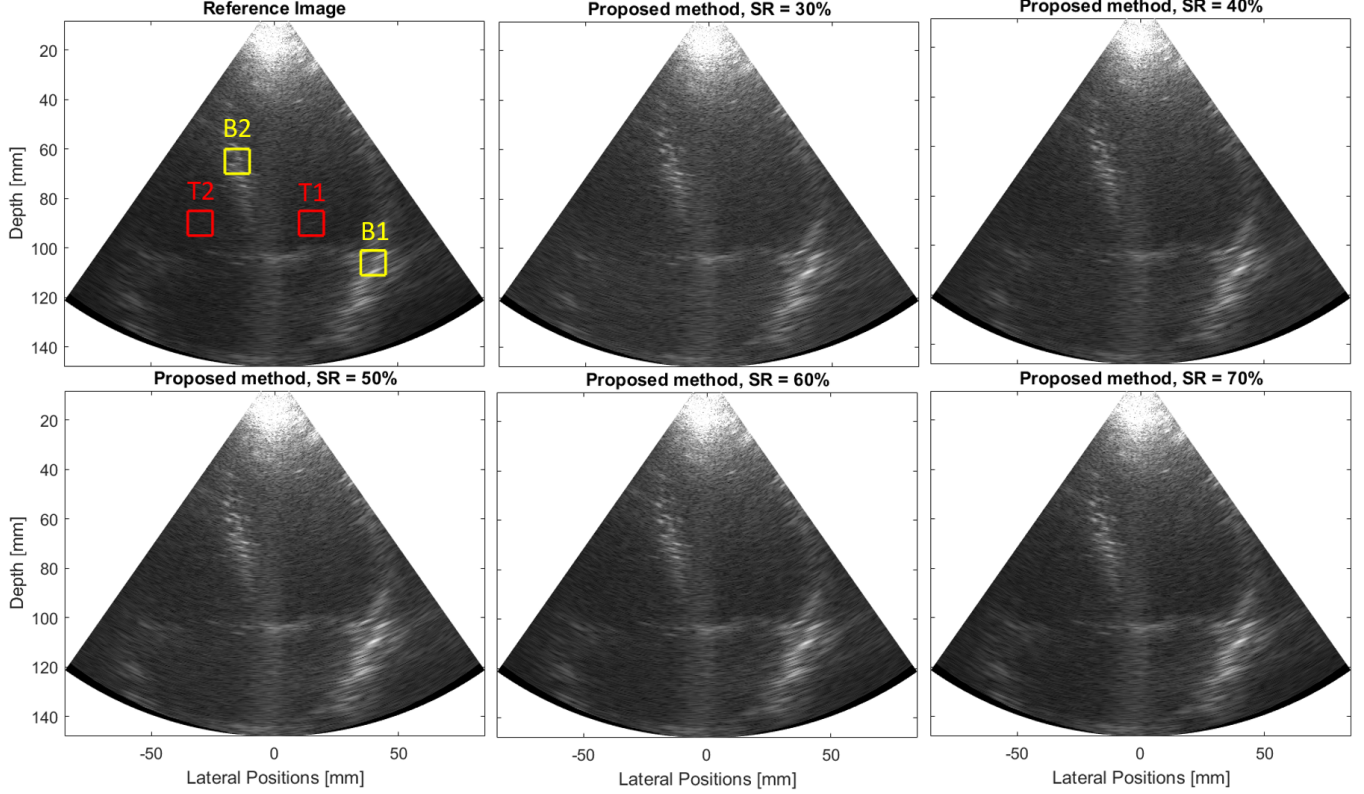


Fig. 8. Original *in vivo* cardiac image and the images reconstructed by the proposed method with different sampling rate on IQ data. The red and yellow block in the reference image represent the regions used to compute CNR.

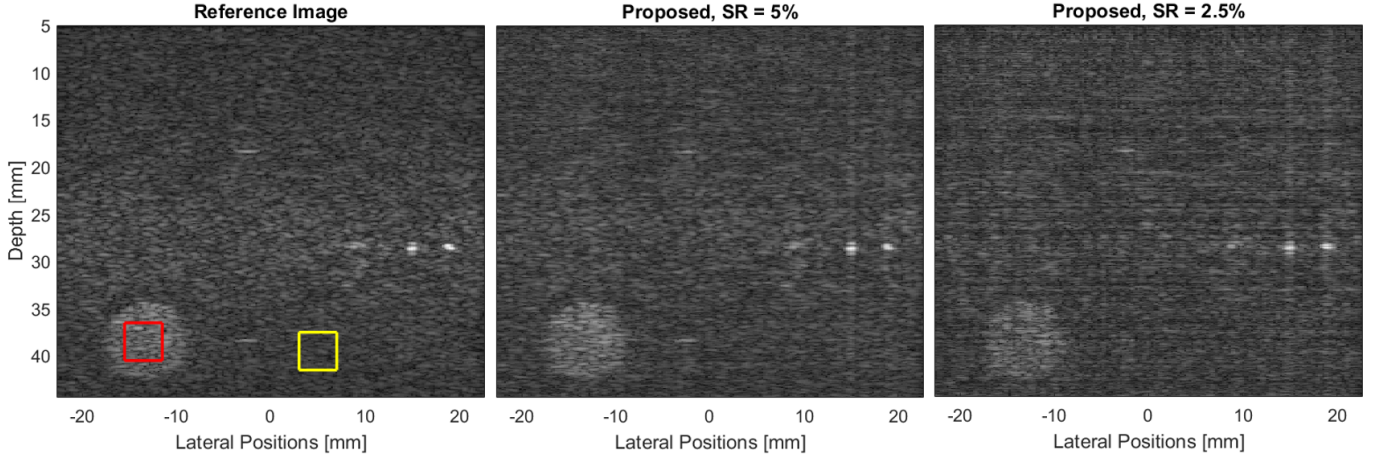


Fig. 9. Original B-mode image and the image reconstructed using the proposed approach with 5% and 2.5% of samples. The red and yellow block in the reference image represent the regions used to compute CNR.

than 0.1 dB. Therefore, it is interesting to investigate how the proposed approach performs in extreme cases, *i.e.* the image quality of the proposed approach with even fewer samples. Figure 9 displays the reference B-mode image and the images reconstructed from the proposed approach using 5% and 2.5% of data samples, respectively. As can be seen, the proposed approach can preserve the main structure of the image even with 2.5% of samples, such as the hyperechoic cyst. However, strong artifacts appear and the image quality is deteriorated. The CNR of the corresponding images are 7.11 dB, 6.67 dB

and 3.15 dB, respectively.

#### B. Reconstruction time

As can be seen from Figure 5, for a given data, the number of iterations is much related to the tolerance of the stopping criterion, *i.e.* a smaller tolerance requires more iterations to converge. For a given stopping condition (*i.e.*  $5e^{-4}$  in this paper), the computation time for the proposed SDMM-based algorithm is proportional to the total data size of the original signals and inversely proportional to the sampling

rate. With the same sampling rate, the bigger the original data size, the more variables need to be recovered and the SVD decomposition in *Step 2.1* of the optimization algorithm takes more time in each iteration. For example, with the *in vivo* RF dataset in Figure 7 (matrix size  $4838 \times 4544$ ) and 40% of samples, it takes about 3 hours to recover the whole dataset in Matlab 2017a (The Mathworks, Inc. Natick, MA, USA) on LENOVO Ideapad 700 (Intel CORE i7-6700 HQ CPU @ 2.60 GHz, 16 GB RAM) while it takes about 30 minutes for the IQ dataset (matrix size  $692 \times 4544$ ). The computation time could also be reduced by avoiding SVD decompositions like [29]. Similarly, with the same data size, it can also be observed from Figure 5 that the number of iterations is inversely proportional to the sampling rate, *i.e.* the smaller the sampling rate, the more variables need to be recovered and the algorithm needs more iterations to converge. In addition, the current implementation solves exactly the intermediate optimization problems at each iteration. It could also be sped up with partial updates where the cost function is reduced at each iteration, but not minimized. The computational time can be further reduced by using graphics processing unit (GPU).

## VI. CONCLUSION

This paper introduces a new strategy to modeling and reducing the sampling rate based on the low-rank and joint-sparse structure between the US signals from different channels and transmissions. A SDMM-based optimization algorithm is thus proposed to efficiently solve the resulting problem. Simulations, phantom experiments and *in vivo* experiments were performed to validate and evaluate the proposed method. The results demonstrate that the proposed approach is capable of reconstructing the whole image from a sparse set of samples (*e.g.* 10% of samples) while keeping adequate image quality.

## ACKNOWLEDGMENT

This work was supported in part by the European Research Council under the European Union's Seventh Framework Program (HeartMAPAS: FP7/2007-2013/ERC) under Grant 281748. This work was also supported by FWO projects G028015N and G090117N; ERC project 258581; and FNRS-FWO EOS project 30468160 "Structured low-rank matrix / tensor approximation: numerical optimization-based algorithms and applications".

## APPENDIX

To better illustrate the low-rank and joint-sparse property of the ultrasound rawdata, we take the simulated data of Figure 2 in the paper as an example. For this dataset, the size of  $\mathbf{X}$  is  $1948 \times 6400$ , *i.e.*  $M$  is 1948 (the number of time samples along depth for each channel) and  $N$  is 6400 (the total number of received channels for one image). Under the assumption that the band width of the transmitter is 1, then  $k = 2 * f_0 / f_s \approx 546$ . Figure 10 shows the amplitudes of each column of  $\mathbf{D}$ . For samples around the center, the amplitudes are zero. This corresponds to rows of zeros in the  $\mathbf{D}$  matrix and justifies the use of the joint-sparsity prior  $\|\mathbf{D}\|_{2,1}$  in problem (8). Figure

11 shows the singular values of  $\mathbf{D}$ . From this figure, we can see that the  $\text{rank}(\mathbf{D})$  is around 400. Thus we have the relation  $\text{rank}(\mathbf{X}) < k < N$  and we use the nuclear norm term  $\|\mathbf{D}\|_*$  in (8).

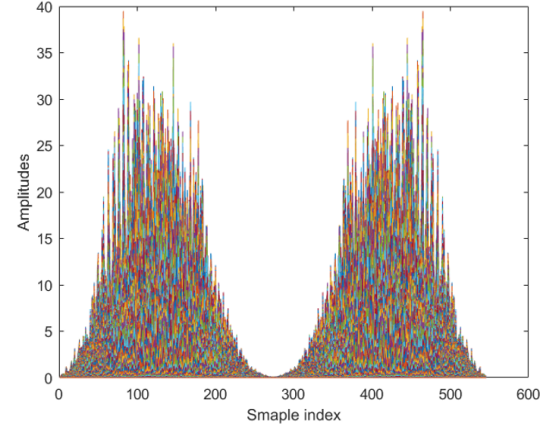


Fig. 10. Amplitudes of each column of  $\mathbf{D}$ .

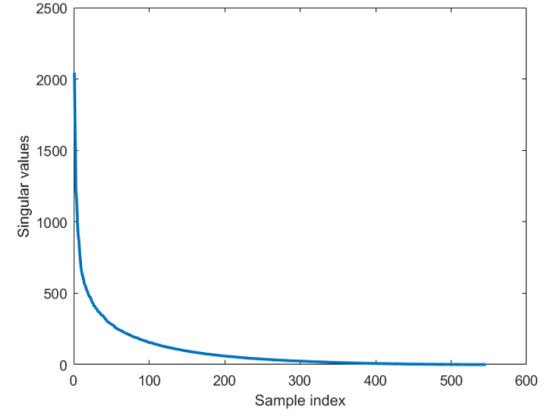


Fig. 11. Singular values of  $\mathbf{D}$ .

## REFERENCES

- [1] B. D. Steinberg, "Digital beamforming in ultrasound," *IEEE Transactions on ultrasonics, ferroelectrics, and frequency control*, vol. 39, no. 6, pp. 716–721, 1992.
- [2] D. L. Donoho, "Compressed sensing," *IEEE Transactions on information theory*, vol. 52, no. 4, pp. 1289–1306, 2006.
- [3] E. J. Candès, J. Romberg, and T. Tao, "Robust uncertainty principles: Exact signal reconstruction from highly incomplete frequency information," *IEEE Transactions on information theory*, vol. 52, no. 2, pp. 489–509, 2006.
- [4] E. J. Candès and M. B. Wakin, "An introduction to compressive sampling," *IEEE signal processing magazine*, vol. 25, no. 2, pp. 21–30, 2008.
- [5] J. Liu, Q. He, and J. Luo, "A compressed sensing strategy for synthetic transmit aperture ultrasound imaging," *IEEE transactions on medical imaging*, vol. 36, no. 4, pp. 878–891, 2017.
- [6] C. Quinsac, A. Basarab, and D. Kouamé, "Frequency domain compressive sampling for ultrasound imaging," *Advances in Acoustics and Vibration*, vol. 2012, 2012.
- [7] C. Quinsac, A. Basarab, J.-M. Girault, and D. Kouamé, "Compressed sensing of ultrasound images: Sampling of spatial and frequency domains," in *Signal Processing Systems (SIPS), 2010 IEEE Workshop on*. IEEE, 2010, pp. 231–236.

- [8] O. Lorintiu, H. Liebgott, M. Alessandrini, O. Bernard, and D. Friboulet, "Compressed sensing reconstruction of 3d ultrasound data using dictionary learning and line-wise subsampling," *IEEE transactions on medical imaging*, vol. 34, no. 12, pp. 2467–2477, 2015.
- [9] J. Liu, Q. He, and J. Luo, "Compressed sensing based synthetic transmit aperture imaging: Validation in a convex array configuration," *IEEE Transactions on Ultrasonics, Ferroelectrics, and Frequency Control*, 2018, *in press*.
- [10] D. Friboulet, H. Liebgott, and R. Prost, "Compressive sensing for raw rf signals reconstruction in ultrasound," in *Ultrasonics Symposium (IUS), 2010 IEEE*. IEEE, 2010, pp. 367–370.
- [11] R. Tur, Y. C. Eldar, and Z. Friedman, "Innovation rate sampling of pulse streams with application to ultrasound imaging," *IEEE Transactions on Signal Processing*, vol. 59, no. 4, pp. 1827–1842, 2011.
- [12] N. Wagner, Y. C. Eldar, A. Feuer, G. Danin, and Z. Friedman, "Xampling in ultrasound imaging," *arXiv preprint arXiv:1104.5327*, 2011.
- [13] M. F. Schiffner and G. Schmitz, "Fast pulse-echo ultrasound imaging employing compressive sensing," in *Ultrasonics Symposium (IUS), 2011 IEEE International*. IEEE, 2011, pp. 688–691.
- [14] H. Liebgott, R. Prost, and D. Friboulet, "Pre-beamformed rf signal reconstruction in medical ultrasound using compressive sensing," *Ultrasound*, vol. 53, no. 2, pp. 525–533, 2013.
- [15] N. Wagner, Y. C. Eldar, and Z. Friedman, "Compressed beamforming in ultrasound imaging," *IEEE Transactions on Signal Processing*, vol. 60, no. 9, pp. 4643–4657, 2012.
- [16] T. Chernyakova and Y. Eldar, "Fourier-domain beamforming: the path to compressed ultrasound imaging," *IEEE transactions on ultrasonics, ferroelectrics, and frequency control*, vol. 61, no. 8, pp. 1252–1267, 2014.
- [17] A. Achim, B. Buxton, G. Tzagkarakis, and P. Tsakalides, "Compressive sensing for ultrasound rf echoes using a-stable distributions," in *Engineering in Medicine and Biology Society (EMBC), 2010 Annual International Conference of the IEEE*. IEEE, 2010, pp. 4304–4307.
- [18] X. Zhuang, Y. Zhao, Z. Dai, H. Wang, and L. Wang, "Ultrasonic signal compressive detection with sub-nyquist sampling rate," 2012.
- [19] J. Zhou, Y. He, M. Chirala, B. M. Sadler, and S. Hoyos, "Compressed digital beamformer with asynchronous sampling for ultrasound imaging," in *Acoustics, Speech and Signal Processing (ICASSP), 2013 IEEE International Conference on*. IEEE, 2013, pp. 1056–1060.
- [20] A. Basarab, H. Liebgott, O. Bernard, D. Friboulet, and D. Kouamé, "Medical ultrasound image reconstruction using distributed compressive sampling," in *Biomedical Imaging (ISBI), 2013 IEEE 10th International Symposium on*. IEEE, 2013, pp. 628–631.
- [21] G. David, J.-l. Robert, B. Zhang, and A. F. Laine, "Time domain compressive beam forming of ultrasound signals," *The Journal of the Acoustical Society of America*, vol. 137, no. 5, pp. 2773–2784, 2015.
- [22] A. Besson, D. Perdios, F. Martinez, Z. Chen, R. E. Carrillo, M. Ardit, Y. Wiaux, and J.-P. Thiran, "Ultrafast ultrasound imaging as an inverse problem: Matrix-free sparse image reconstruction," *IEEE transactions on ultrasonics, ferroelectrics, and frequency control*, vol. 65, no. 3, pp. 339–355, 2018.
- [23] D. Baron, M. F. Duarte, M. B. Wakin, S. Sarvotham, and R. G. Baraniuk, "Distributed compressive sensing," *arXiv preprint arXiv:0901.3403*, 2009.
- [24] Q. Zhang, B. Li, and M. Shen, "A measurement-domain adaptive beamforming approach for ultrasound instrument based on distributed compressed sensing: initial development," *Ultrasonics*, vol. 53, no. 1, pp. 255–264, 2013.
- [25] K. H. Jin, Y. S. Han, and J. C. Ye, "Compressive dynamic aperture b-mode ultrasound imaging using annihilating filter-based low-rank interpolation," in *Biomedical Imaging (ISBI), 2016 IEEE 13th International Symposium on*. IEEE, 2016, pp. 1009–1012.
- [26] E. J. Candès and B. Recht, "Exact matrix completion via convex optimization," *Foundations of Computational mathematics*, vol. 9, no. 6, p. 717, 2009.
- [27] A. Balachandrasekaran, G. Ongie, and M. Jacob, "Accelerated dynamic mri using structured low rank matrix completion," in *Image Processing (ICIP), 2016 IEEE International Conference on*. IEEE, 2016, pp. 1858–1862.
- [28] X. Hu, N. Tong, J. Wang, S. Ding, and X. Zhao, "Matrix completion-based mimo radar imaging with sparse planar array," *Signal Processing*, vol. 131, pp. 49–57, 2017.
- [29] H. Lu, X. Zhang, T. Qiu, J. Yang, J. Ying, D. Guo, Z. Chen, and X. Qu, "Low rank enhanced matrix recovery of hybrid time and frequency data in fast magnetic resonance spectroscopy," *IEEE Transactions on Biomedical Engineering*, 2017.
- [30] H. Zhang, V. M. Patel, and R. Chellappa, "Robust multimodal recognition via multitask multivariate low-rank representations," in *Automatic Face and Gesture Recognition (FG), 2015 11th IEEE International Conference and Workshops on*, vol. 1. IEEE, 2015, pp. 1–8.
- [31] M. Golbabaei and P. Vandergheynst, "Hyperspectral image compressed sensing via low-rank and joint-sparse matrix recovery," in *Acoustics, Speech and Signal Processing (ICASSP), 2012 IEEE International Conference on*. Ieee, 2012, pp. 2741–2744.
- [32] T. Gelvez, H. Rueda, and H. Arguello, "Joint sparse and low rank recovery algorithm for compressive hyperspectral imaging," *Applied optics*, vol. 56, no. 24, pp. 6785–6795, 2017.
- [33] H. Zhang, V. M. Patel, and R. Chellappa, "Low-rank and joint sparse representations for multi-modal recognition," *IEEE Transactions on Image Processing*, vol. 26, no. 10, pp. 4741–4752, 2017.
- [34] S. Setzer, G. Steidl, and T. Teuber, "Deblurring poissonian images by split bregman techniques," *Journal of Visual Communication and Image Representation*, vol. 21, no. 3, pp. 193–199, 2010.
- [35] T. Goldstein and S. Osher, "The split bregman method for l1-regularized problems," *SIAM journal on imaging sciences*, vol. 2, no. 2, pp. 323–343, 2009.
- [36] Z. Chen, A. Basarab, and D. Kouamé, "Reconstruction of enhanced ultrasound images from compressed measurements using simultaneous direction method of multipliers," *IEEE transactions on ultrasonics, ferroelectrics, and frequency control*, vol. 63, no. 10, pp. 1525–1534, 2016.
- [37] M. Golbabaei and P. Vandergheynst, "Compressed sensing of simultaneous low-rank and joint-sparse matrices," *arXiv preprint arXiv:1211.5058*, 2012.
- [38] A. Gogna, A. Shukla, H. Agarwal, and A. Majumdar, "Split bregman algorithms for sparse/joint-sparse and low-rank signal recovery: Application in compressive hyperspectral imaging," in *Image Processing (ICIP), 2014 IEEE International Conference on*. IEEE, 2014, pp. 1302–1306.
- [39] M. Fornasier and H. Rauhut, "Recovery algorithms for vector-valued data with joint sparsity constraints," *SIAM Journal on Numerical Analysis*, vol. 46, no. 2, pp. 577–613, 2008.
- [40] J.-F. Cai, E. J. Candès, and Z. Shen, "A singular value thresholding algorithm for matrix completion," *SIAM Journal on Optimization*, vol. 20, no. 4, pp. 1956–1982, 2010.
- [41] Y. Hu, D. Zhang, J. Ye, X. Li, and X. He, "Fast and accurate matrix completion via truncated nuclear norm regularization," *IEEE transactions on pattern analysis and machine intelligence*, vol. 35, no. 9, pp. 2117–2130, 2013.
- [42] E. J. Candès, X. Li, Y. Ma, and J. Wright, "Robust principal component analysis?" *Journal of the ACM (JACM)*, vol. 58, no. 3, p. 11, 2011.
- [43] S. Shekhar, V. M. Patel, N. M. Nasrabadi, and R. Chellappa, "Joint sparse representation for robust multimodal biometrics recognition," *IEEE Transactions on Pattern Analysis and Machine Intelligence*, vol. 36, no. 1, pp. 113–126, 2014.
- [44] E. J. Candes, "The restricted isometry property and its implications for compressed sensing," *Comptes rendus mathematique*, vol. 346, no. 9–10, pp. 589–592, 2008.
- [45] E. van den Berg and M. P. Friedlander, "SPGL1: A solver for large-scale sparse reconstruction," June 2007, <http://www.cs.ubc.ca/labs/scl/spgl1>.
- [46] C. Schretter, S. Bundervoet, D. Blinder, A. Dooms, J. D'hooge, and P. Schelkens, "Ultrasound imaging from sparse rf samples using system point spread functions," *IEEE transactions on ultrasonics, ferroelectrics, and frequency control*, vol. 65, no. 3, pp. 316–326, 2018.
- [47] J. A. Jensen, "Field: A program for simulating ultrasound systems," in *10TH NORDICBALTIC CONFERENCE ON BIOMEDICAL IMAGING, VOL. 4, SUPPLEMENT 1, PART 1: 351–353*. Citeseer, 1996.
- [48] M. Zhang, F. Varay, A. Besson, R. E. Carrillo, M. Viallon, D. Garcia, J.-P. Thiran, D. Friboulet, H. Liebgott, and O. Bernard, "Extension of fourier-based techniques for ultrafast imaging in ultrasound with diverging waves," *IEEE transactions on ultrasonics, ferroelectrics, and frequency control*, vol. 63, no. 12, pp. 2125–2137, 2016.
- [49] A. Ortega, D. Lines, J. Pedrosa, B. Chakraborty, V. Komini, H. Gassert, and J. D'hooge, "Hd-pulse: High channel density programmable ultrasound system based on consumer electronics," in *Ultrasonics Symposium (IUS), 2015 IEEE International*. IEEE, 2015, pp. 1–3.